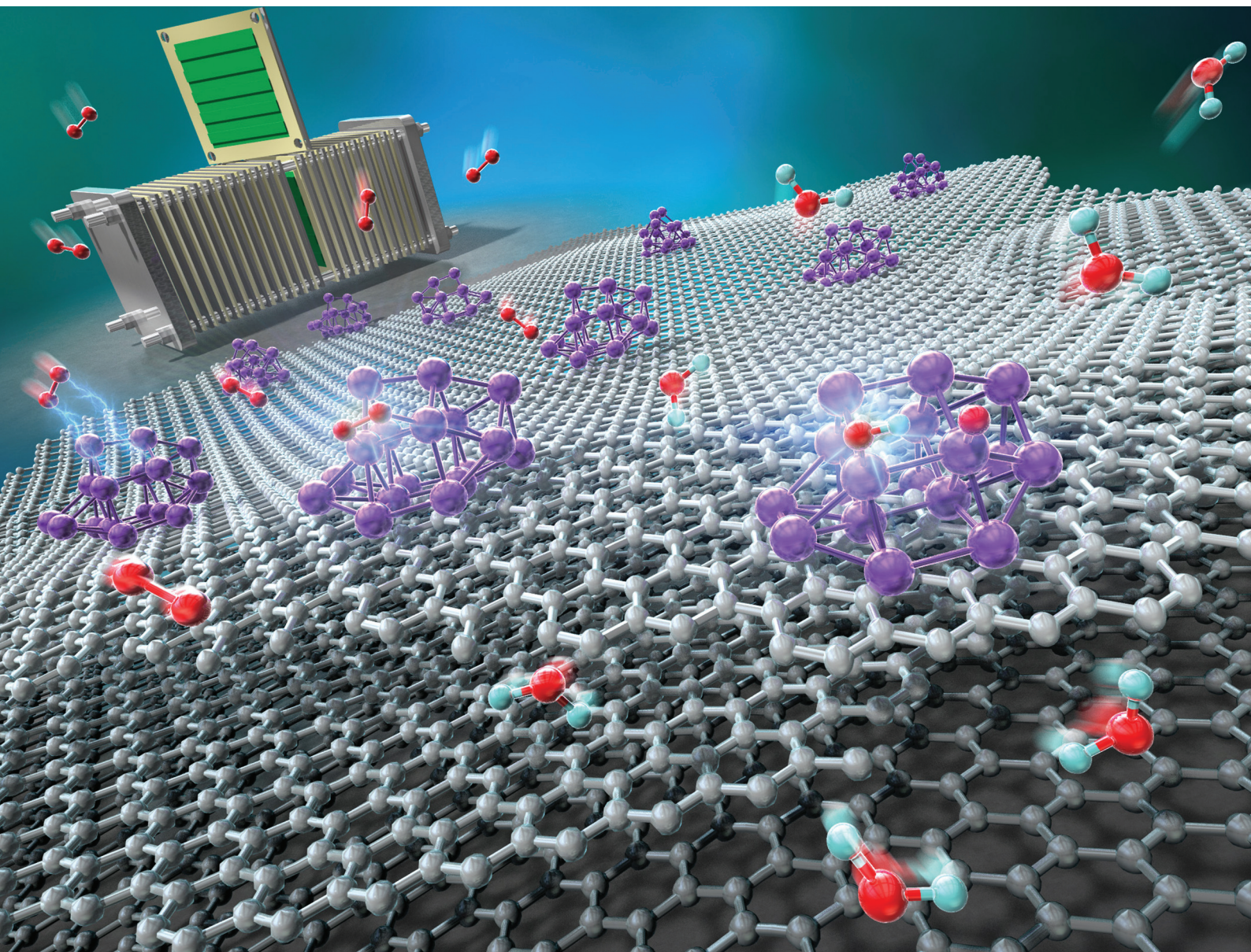


# Nanoscale

rsc.li/nanoscale



ISSN 2040-3372

**PAPER**

Kenji Iida, Yuichi Negishi *et al.*  
Pt<sub>17</sub> nanocluster electrocatalysts: preparation and origin of  
high oxygen reduction reaction activity





Cite this: *Nanoscale*, 2023, **15**, 7272

# Pt<sub>17</sub> nanocluster electrocatalysts: preparation and origin of high oxygen reduction reaction activity†

Tokuhisa Kawawaki,<sup>a</sup> Yusuke Mitomi,<sup>a</sup> Naoki Nishi,<sup>a</sup> Ryuki Kurosaki,<sup>a</sup> Kazutaka Oiwa,<sup>a</sup> Tomoya Tanaka,<sup>a</sup> Hinoki Hirase,<sup>d</sup> Sayuri Miyajima,<sup>a</sup> Yoshiki Niihori,<sup>b</sup> D. J. Osborn,<sup>f</sup> Takanori Koitaya,<sup>c,e</sup> Gregory F. Metha,<sup>f</sup> Toshihiko Yokoyama,<sup>c,e</sup> Kenji Iida<sup>\*d</sup> and Yuichi Negishi<sup>†a,b</sup>

We recently found that [Pt<sub>17</sub>(CO)<sub>12</sub>(PPh<sub>3</sub>)<sub>8</sub>]<sup>z</sup> (Pt = platinum; CO = carbon monoxide; PPh<sub>3</sub> = triphenylphosphine; z = 1+ or 2+) is a Pt nanocluster (Pt NC) that can be synthesized with atomic precision in air. The present study demonstrates that it is possible to prepare a Pt<sub>17</sub>-supported carbon black (CB) catalyst (Pt<sub>17</sub>/CB) with 2.1 times higher oxygen reduction reaction (ORR) activity than commercial Pt nanoparticles/CB by the adsorption of [Pt<sub>17</sub>(CO)<sub>12</sub>(PPh<sub>3</sub>)<sub>8</sub>]<sup>z</sup> onto CB and subsequent calcination of the catalyst. Density functional theory calculation strongly suggests that the high ORR activity of Pt<sub>17</sub>/CB originates from the surface Pt atoms that have an electronic structure appropriate for the progress of ORR. These results are expected to provide design guidelines for the fabrication of highly active ORR catalysts using Pt NCs with a diameter of about 1 nm and thereby enabling the use of reduced amounts of Pt in polymer electrolyte fuel cells.

Received 13th March 2023,  
Accepted 23rd March 2023

DOI: 10.1039/d3nr01152f

[rsc.li/nanoscale](http://rsc.li/nanoscale)

## Introduction

As an option to tackle the issues of the depletion of fossil resources and global warming, our society is expected to shift from using fossil resources to using alternative sustainable energy sources such as hydrogen (H<sub>2</sub>) (Fig. S1†). The energy conversion system based on H<sub>2</sub> involves a polymer electrolyte fuel cell (PEFC; Fig. S2†), a power generation device that produces electricity from H<sub>2</sub> and oxygen (O<sub>2</sub>). However, current PEFCs use a large amount of platinum (Pt), which makes them expensive to manufacture and run. Though cost reduction can be achieved by improving parts other than the Pt catalyst, the

continuous use of large amounts of Pt would result in a shortage of Pt. Therefore, for a sustainable hydrogen energy society, it is essential to reduce the amount of Pt used in PEFC electrocatalysts (Fig. S2†).

In PEFCs, the oxygen reduction reaction (ORR) at the cathode is the rate-determining reaction, and catalysts with Pt nanoparticles (Pt NPs) of 2–3 nm in diameter supported on carbon black (Pt NPs/CB) are widely used for such cathode catalysts. However, studies by Yamamoto and co-workers,<sup>1,2</sup> Nakajima and co-workers,<sup>3</sup> and Fischer and co-workers<sup>4</sup> have shown that Pt nanoclusters (NCs) of ~1 nm in size exhibit higher ORR activity than Pt NPs of 2–3 nm in size. It is thus expected that the use of precisely synthesized Pt NCs of ~1 nm in size as ORR electrocatalysts would afford reduced amounts of Pt to be used in PEFCs.

Pt NCs and their alloy NCs of ~1 nm in size can be synthesized with atomic precision when carbon monoxide (CO)<sup>5,6</sup> and phosphine (PR<sub>3</sub>) are used as ligands (Pt<sub>n</sub>(CO)<sub>m</sub>(PR<sub>3</sub>)<sub>l</sub>; n, m, l = the number of Pt atom, CO ligand, and PR<sub>3</sub> ligand, respectively).<sup>7–9</sup> However, most of the Pt<sub>n</sub>(CO)<sub>m</sub>(PR<sub>3</sub>)<sub>l</sub> NCs reported to date face stability issues under atmospheric conditions,<sup>7–9</sup> and consequently few studies have been conducted on their application as ORR electrocatalysts. We recently found that [Pt<sub>17</sub>(CO)<sub>12</sub>(PPh<sub>3</sub>)<sub>8</sub>]<sup>z</sup> (z = 1+ or 2+; PPh<sub>3</sub> = triphenylphosphine; Fig. 1(a), S3(a) and (b)†) is a Pt<sub>n</sub>(CO)<sub>m</sub>(PR<sub>3</sub>)<sub>l</sub> NC that can be synthesized and stable in air.<sup>10–12</sup> This NC has a Pt core of ~1 nm and can be isolated with atomic precision by a combination of simple operations:

<sup>a</sup>Department of Applied Chemistry, Faculty of Science, Tokyo University of Science, Kagurazaka, Shinjuku-ku, Tokyo 162-8601, Japan. E-mail: Kawawaki@rs.tus.ac.jp, negishi@rs.tus.ac.jp; Fax: +81-3-5261-4631; Tel: +81-3-5228-9145

<sup>b</sup>Research Institute for Science & Technology, Tokyo University of Science, Kagurazaka, Shinjuku-ku, Tokyo 162-8601, Japan

<sup>c</sup>Physical and Chemical Research Infrastructure Group, RIKEN SPring-8 Center, RIKEN, Sayo, Hyogo 679-5198, Japan

<sup>d</sup>Institute for Catalysis, Hokkaido University, Sapporo, Hokkaido 001-0021, Japan

<sup>e</sup>Institute for Molecular Science, Okazaki, Aichi 444-8585, Japan

<sup>f</sup>Department of Chemistry, University of Adelaide, Adelaide, South Australia, 5005, Australia

†Electronic supplementary information (ESI) available: Experimental section (Fig. S36–S39), calculation method, additional tables, additional figures, additional MALDI-MS, FT-IR, XPS, EXAFS spectra, TEM images, TG curves, CV, LSV curves, and optimized structures. See DOI: <https://doi.org/10.1039/d3nr01152f>

‡These authors contributed equally.



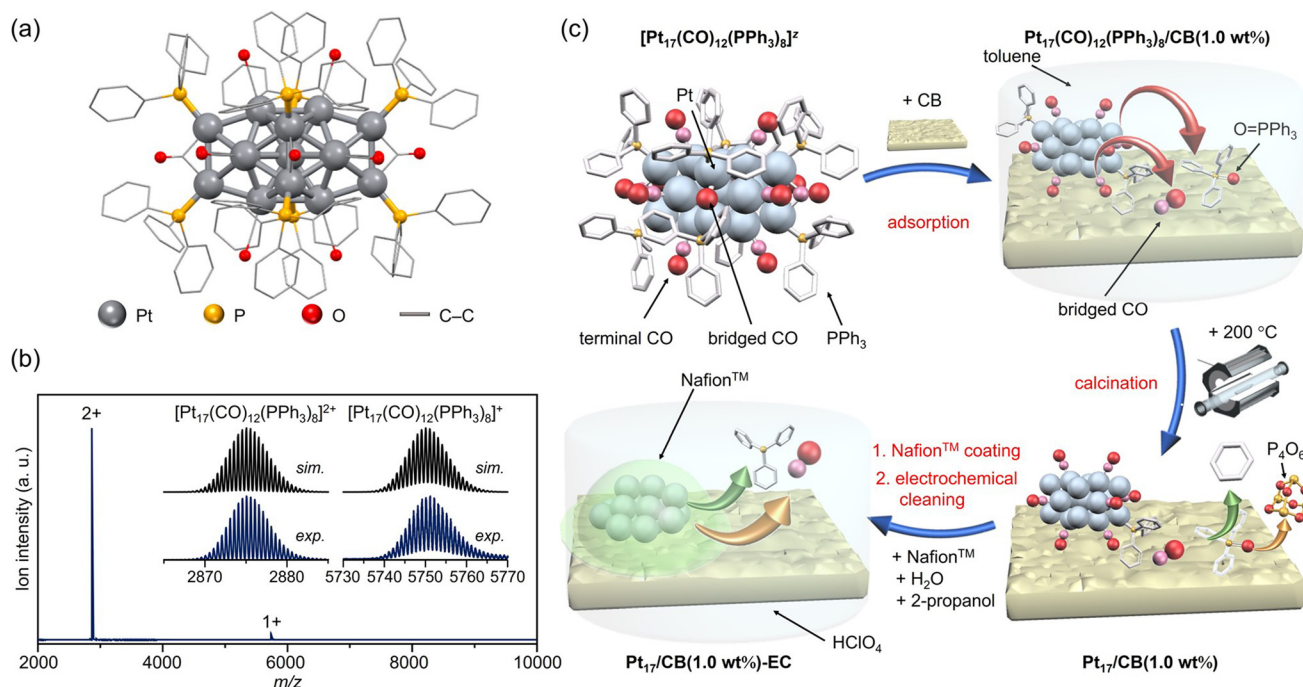


**Fig. 1** Preparation of  $\text{Pt}_{17}/\text{CB}$ . (a) Geometric structure and (b) ESI-MS spectrum of precursor  $[\text{Pt}_{17}(\text{CO})_{12}(\text{PPh}_3)_8]^{2+}$ . (c) Schematic of the preparation procedure: adsorption of  $[\text{Pt}_{17}(\text{CO})_{12}(\text{PPh}_3)_8]^{2+}$  onto CB, calcination of the catalyst at  $200^\circ\text{C}$ , and slurry preparation. In (c), the states of the ligand at each stage are estimated based on the results of the FT-IR spectroscopy (Fig. 3 and S10†), HAX-PES (Fig. S11†), FT-EXAFS (Fig. 4(a)), XANES (Fig. 4(b)), and TGA (Fig. S18†) analyses.

mixing reagents in air, heating the solvent, and washing the by-products. Furthermore,  $\text{Pt}_{17}$  is located in the size region showing the highest ORR activity.<sup>1,2</sup> Using  $[\text{Pt}_{17}(\text{CO})_{12}(\text{PPh}_3)_8]^{2+}$  as a precursor is expected to enable the preparation of highly active ORR electrocatalysts with  $\text{Pt}_{17}$  ( $\sim 1$  nm in size) supported on CB ( $\text{Pt}_{17}/\text{CB}$ ). As only 17 Pt atoms are included in  $\text{Pt}_{17}/\text{CB}$ , it is expected that density functional theory (DFT) calculations<sup>13</sup> of  $\text{Pt}_{17}/\text{CB}$  can be used to elucidate the origin of the high activity of the catalyst.

In the present study, we aim to (1) engineer ORR electrocatalysts with a higher activity than that of commercial Pt NPs/CB loaded with Pt NPs of 2–3 nm in size using  $[\text{Pt}_{17}(\text{CO})_{12}(\text{PPh}_3)_8]^{2+}$  as a precursor, and (2) elucidate the origin of the high ORR shown by Pt NCs of  $\sim 1$  nm in size by DFT calculations. As a result, we have succeeded in fabricating  $\text{Pt}_{17}/\text{CB}$  catalyst with an ORR activity 2.1 times higher than that of commercial Pt NPs/CB. The DFT calculations strongly suggest the origin of the high activity to be attributed to the surface Pt atoms which have an electronic structure appropriate for ORR.

## Results and discussion

### Preparation of $\text{Pt}_{17}/\text{CB}$ ORR electrocatalyst using atomically precise $[\text{Pt}_{17}(\text{CO})_{12}(\text{PPh}_3)_8]\text{Cl}_n$

The  $[\text{Pt}_{17}(\text{CO})_{12}(\text{PPh}_3)_8]^{2+}$  ( $[\text{Pt}_{17}(\text{CO})_{12}(\text{PPh}_3)_8]\text{Cl}_n$ ;  $n = 1$  or  $2$ ) precursor was synthesized by polyol reduction<sup>14–20</sup> as in our previous reports.<sup>11</sup> In the synthesis, an ethylene glycol solution

containing Pt salts and sodium hydroxide was first heated in air. The temperature of the solution was then cooled to room temperature, and a mixture of  $\text{Pt}_n(\text{CO})_m(\text{PR}_3)_l$  NCs was prepared by adding  $\text{PPh}_3$  to the solution. From the resulting mixture, only  $[\text{Pt}_{17}(\text{CO})_{12}(\text{PPh}_3)_8]^{2+}$  ( $z = 1+$  or  $2+$ ) was separated by solvent extraction. In the present study,  $[\text{Pt}_{17}(\text{CO})_{12}(\text{PPh}_3)_8]^{2+}$  was successfully obtained with 3.8 times higher yield than that in our previous report<sup>11</sup> by optimizing each parameter (Fig. S4†; e.g., Pt salt concentration, stirring time, amount of added  $\text{PPh}_3$ ) in a series of operations (Fig. S5†). The obtained product contained  $[\text{Pt}_{17}(\text{CO})_{12}(\text{PPh}_3)_8]^{2+}$  with atomic precision, as confirmed by electrospray ionization mass spectrometry (ESI-MS; Fig. 1(b)).

According to recent DFT studies,<sup>21</sup>  $\text{Pt}_n(\text{CO})_m(\text{PR}_3)_l$  NCs can be stabilized and isolated when the total number of valence electrons satisfies the closed shell electronic structure. In the case of  $\text{Pt}_{17}(\text{CO})_{12}(\text{PR}_3)_8$ ,  $[\text{Pt}_{17}(\text{CO})_{12}(\text{PR}_3)_8]^0$  has been isolated in anaerobic synthetic studies because it satisfies the closed shell electronic structure ( $1s^2 1p^6$ ) of the superatom at neutral state (Fig. S3(c)†).<sup>9</sup> Our results demonstrate that (1)  $[\text{Pt}_{17}(\text{CO})_{12}(\text{PR}_3)_8]^0$  could be oxidized in atmosphere similarly to other  $\text{Pt}_n(\text{CO})_m(\text{PR}_3)_l$  NCs,<sup>7–9</sup> and (2) unlike other  $\text{Pt}_n(\text{CO})_m(\text{PR}_3)_l$  NCs,  $[\text{Pt}_{17}(\text{CO})_{12}(\text{PR}_3)_8]^{2+}$  ( $z = 1+$  or  $2+$ ), which does not satisfy the closed shell electronic structure, was isolated.  $[\text{Pt}_{17}(\text{CO})_{12}(\text{PR}_3)_8]^0$  is also geometrically stabilized by the inclusion of an icosahedral metal core in the framework structure, which is a common feature in stable NCs.<sup>22–32</sup> This seems to be the reason why  $[\text{Pt}_{17}(\text{CO})_{12}(\text{PPh}_3)_8]^0$  could main-



tain its framework structure even when oxidized in air, unlike the case of other  $\text{Pt}_n(\text{CO})_m(\text{PR}_3)_l$  NCs, and  $[\text{Pt}_{17}(\text{CO})_{12}(\text{PPh}_3)_8]^z$  ( $z = 1+$  or  $2+$ ) selectively formed during operation in air. The high framework stability against oxidation is similar to that of  $[\text{Au}_{25}(\text{SR})_{18}]^z$  ( $\text{Au} = \text{gold}$ ;  $\text{SR} = \text{thiolate}$ ;  $z = 1-, 0$  or  $1+$ ), which also has an icosahedral metal core.<sup>23–25</sup>

The resulting  $[\text{Pt}_{17}(\text{CO})_{12}(\text{PPh}_3)_8]^z$  NC (see Fig. 2(a) and S6† for transmission electron microscopy (TEM) images and S7† for high-angle annular dark field scanning TEM (HAADF-STEM) images) was used as a precursor to prepare the  $\text{Pt}_{17}/\text{CB}$  catalysts. In the commercial Pt NPs/CB (TEC10E50E) used as a comparison for activity, Ketjen black, which is known as a highly conductive CB, is used as support.<sup>33</sup> Therefore, in this study, we used Ketjen black (EC300J; hereafter described simply as CB) as a support for  $\text{Pt}_{17}$ , unlike our previous report on ORR.<sup>34</sup>

In the catalyst preparation, CB was first added to a toluene solution of  $[\text{Pt}_{17}(\text{CO})_{12}(\text{PPh}_3)_8]\text{Cl}_n$  and the solution was stirred for 24 h (Fig. 1(c)). The weight ratio of Pt to CB was set to 1.0 wt%. Analysis of the supernatant solution by inductively

coupled plasma (ICP)-MS confirmed that  $[\text{Pt}_{17}(\text{CO})_{12}(\text{PPh}_3)_8]^z$  was adsorbed on CB with an adsorption rate of 98.6%. The CB (Ketjen black) contains hydroxyl and carboxyl groups,<sup>33</sup> and hydrogen bonds are expected to form between these polar functional groups and CO. This seems to be the reason why  $[\text{Pt}_{17}(\text{CO})_{12}(\text{PPh}_3)_8]^z$  adsorbed on CB at a high adsorption rate when they were mixed at a weight ratio of 1.0 wt% Pt. In contrast, when  $[\text{Pt}_{17}(\text{CO})_{12}(\text{PPh}_3)_8]^z$  was mixed with CB at a higher weight ratio, such as 5.0 wt% Pt,  $[\text{Pt}_{17}(\text{CO})_{12}(\text{PPh}_3)_8]^z$  adsorbed on CB at a lower adsorption rate (66.6%). Under such an adsorption condition, it is difficult to control the amount of Pt loaded on the CB, and therefore, the obtained experimental data are not reproducible or reliable. Accordingly, in subsequent experiments,  $\text{Pt}_{17}(\text{CO})_{12}(\text{PPh}_3)_8/\text{CB}$  with 1.0 wt% Pt (hereafter,  $\text{Pt}_{17}(\text{CO})_{12}(\text{PPh}_3)_8/\text{CB}(1.0 \text{ wt\% Pt})$ ) was used for catalyst preparation (Fig. 2(b) and S8† for TEM images and S9† for HAADF-STEM images).

In general, the presence of ligands covering the NCs on the support prevents the approach of reactants and induces a change in the charge state of the NCs, which leads to a decrease in catalytic activity.<sup>35</sup> Therefore, in many cases, ligands have been removed from NCs by calcination<sup>36,37</sup> or other processes during catalyst preparation. The calcination process also plays a role in immobilizing NCs on the support. However, based on the results of the Fourier transform infrared spectroscopy (FT-IR; Fig. 3, S10 and Table S1†) and P 1s hard X-ray photoelectron spectroscopy (HAX-PES; Fig. S11†) analyses, it is assumed that in the present catalyst preparation, part of the  $\text{PPh}_3$  is oxidized to  $\text{O}=\text{PPh}_3$  during adsorption, which is then stripped from the Pt NC surface and transferred onto CB.<sup>38,39</sup> According to the results of the FT-IR spectroscopy analysis (Fig. 3) and Pt  $L_{3\text{-edge}}$  FT extended X-ray absorption fine structure (FT-EXAFS; Fig. 4(a)) analysis, it appears that the remaining unoxidized  $\text{PPh}_3$  migrated to the interface between  $\text{Pt}_{17}$  and CB (Fig. 1(c) and S12†) and thereby most of the  $\text{Pt}_{17}$  surface became bare after the adsorption of  $[\text{Pt}_{17}(\text{CO})_{12}(\text{PPh}_3)_8]$  onto CB. Therefore,  $\text{Pt}_{17}(\text{CO})_{12}(\text{PPh}_3)_8/\text{CB}(1.0 \text{ wt\% Pt})$  was calcined under a relatively mild condition (200 °C) in this study (Fig. 1(c) and S13†).

The Pt  $L_{3\text{-edge}}$  FT-EXAFS spectra of the catalysts after calcination (Fig. 4(a) and Table S2†) displayed distinct peaks in the Pt–Pt ( $\sim 2.7 \text{ \AA}$ ) and Pt–C ( $\sim 1.7 \text{ \AA}$ ) bond regions (Fig. S14†), indicating that the calcination conditions employed caused immobilization of  $\text{Pt}_{17}$  on the CB (Fig. 1(a)). Calcination under the mild condition employed caused minimal increase in the particle size of the Pt NCs (Fig. 2(c) and S15–S17†). However, as indicated by the results in Fig. 3 and 4(a), under these mild conditions, some ligands ( $\text{CO}$ ,  $\text{PPh}_3$ ,  $\text{O}=\text{PPh}_3$ ) remained in the catalyst (interface between  $\text{Pt}_{17}$  and CB or on CB) (Fig. 1(c) and S12†). Nevertheless, given that a higher calcination temperature of 400 °C caused a significant increase in the particle size of the Pt NCs (Fig. S18–S20†), a temperature of 200 °C was considered to be a moderate calcination temperature to prepare the fine Pt NCs-supported CB catalysts using  $[\text{Pt}_{17}(\text{CO})_{12}(\text{PPh}_3)_8]^z$  as a precursor. Pt  $L_{3\text{-edge}}$  X-ray absorption near-edge structure (XANES; Fig. 4(b)) measurements showed

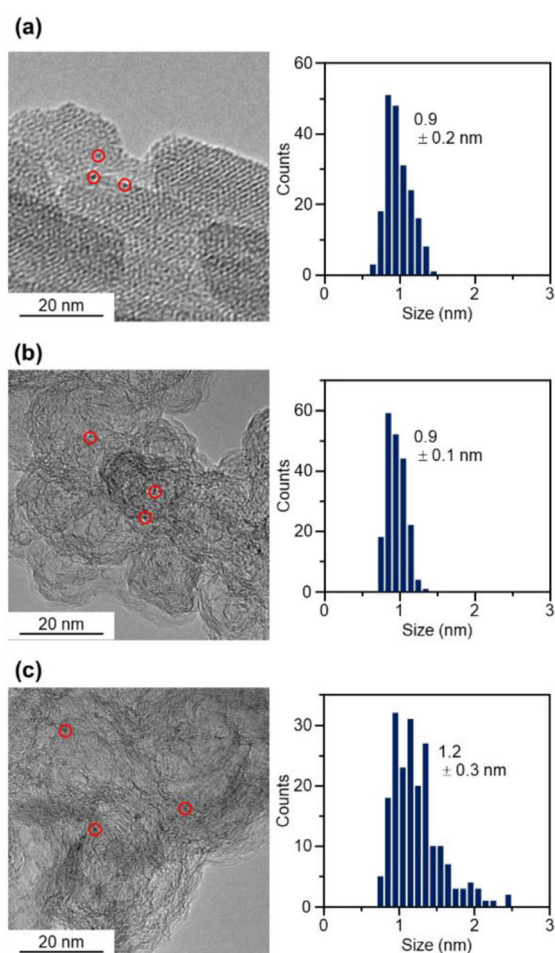


**Fig. 2** TEM images and histograms of each sample. (a)  $[\text{Pt}_{17}(\text{CO})_{12}(\text{PPh}_3)_8]^z$ . (b)  $\text{Pt}_{17}(\text{CO})_{12}(\text{PPh}_3)_8/\text{CB}$ . (c)  $\text{Pt}_{17}/\text{CB}$ . In (a), the parallel lines are not due to the lattice fringes of  $\text{Pt}_{17}$  cluster but due to the collodion membrane on the TEM grid.





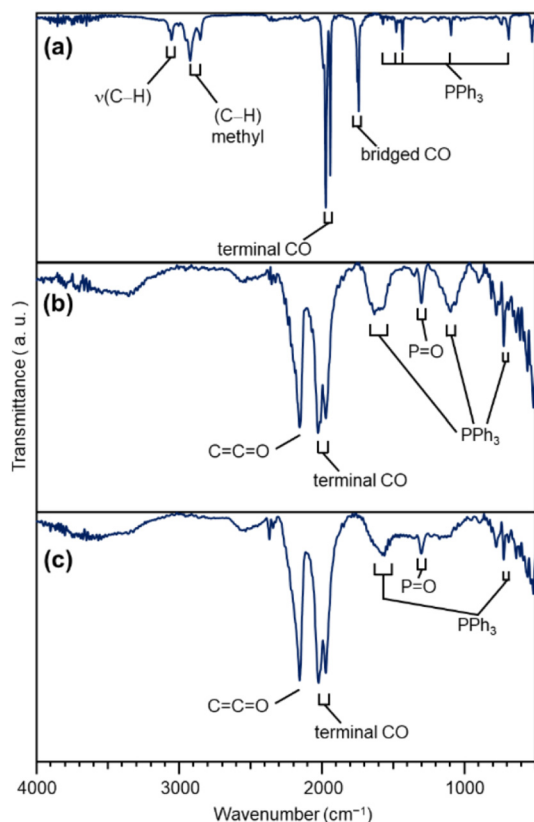


**Fig. 3** FT-IR results of each sample. (a)  $[\text{Pt}_{17}(\text{CO})_{12}(\text{PPh}_3)_8]_2$ . (b)  $\text{Pt}_{17}(\text{CO})_{12}(\text{PPh}_3)_8/\text{CB}$  (1.0 wt% Pt). (c)  $\text{Pt}_{17}/\text{CB}$  (1.0 wt% Pt). In (a), the peaks around  $3000\text{ cm}^{-1}$  are due to 2-methyl-2-butene, which was included in the solvent (dichloromethane) as a stabilizer. Details of the peak assignments are shown in Fig. S10†

that the charge state of Pt is near to Pt(0) in the resulting  $\text{Pt}_{17}/\text{CB}$  (1.0 wt% Pt).

### ORR activity of $\text{Pt}_{17}/\text{CB}$

As described above, calcination at  $200\text{ }^\circ\text{C}$  allows Pt NCs to be loaded on CB while maintaining the particle size of the Pt NCs (Fig. S16†). However, it is assumed that some ligands remain adsorbed on the Pt NC surface when calcined at such a temperature. Therefore, electrochemical cleaning<sup>40,41</sup> of  $\text{Pt}_{17}/\text{CB}$  (1.0 wt% Pt) was performed after slurry preparation to remove remaining ligands from the catalyst ( $\text{Pt}_{17}/\text{CB}$  (1.0 wt% Pt)-EC; Fig. 1(c) and S21†). Only negligible aggregation of  $\text{Pt}_{17}$  was observed after this operation (Fig. S22†), indicating that most of the Pt NCs in  $\text{Pt}_{17}/\text{CB}$  (1.0 wt% Pt)-EC were  $\text{Pt}_{17}$ .

The ORR activity of the catalyst was evaluated by linear sweep voltammetry (LSV).<sup>42–44</sup> In our previous report,<sup>34</sup> we could not obtain the same mass activity for commercial Pt NPs/CB (46.9 wt% Pt) (Fig. S23†) as that reported in the literature ( $170\text{--}180\text{ A g}^{-1}$  for  $0.9\text{ V}$  vs. reversible hydrogen electrode (RHE)).<sup>45</sup> Therefore, in the present study, LSV was conducted under experimental conditions that conform to the Japanese unified standard.<sup>46</sup> As a result, we succeeded in obtaining a

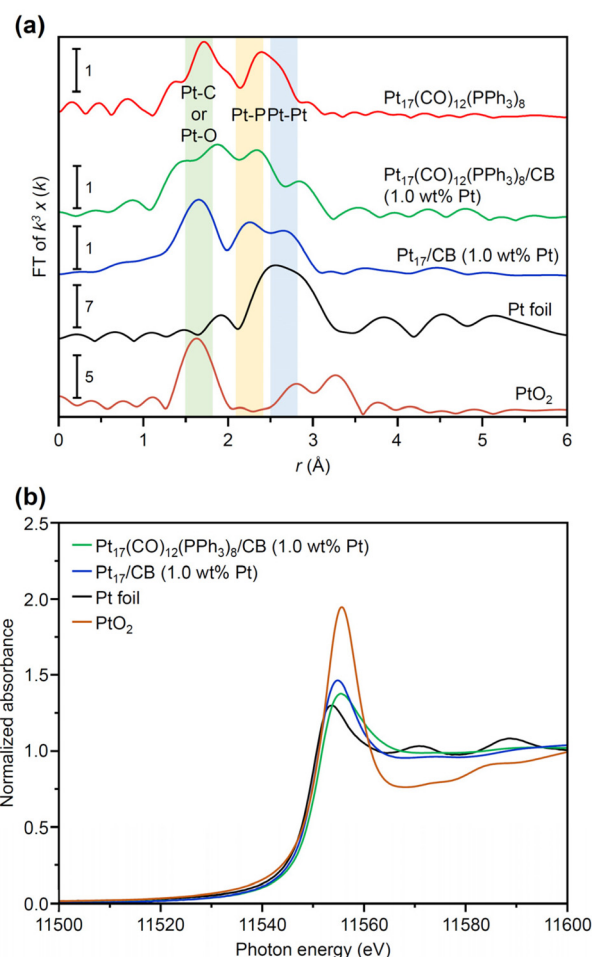


**Fig. 4** XAFS results of each sample. (a) Pt  $L_{3}$ -edge FT-EXAFS of  $\text{Pt}_{17}(\text{CO})_{12}(\text{PPh}_3)_8$ ,  $\text{Pt}_{17}(\text{CO})_{12}(\text{PPh}_3)_8/\text{CB}$  (1.0 wt% Pt),  $\text{Pt}_{17}/\text{CB}$  (1.0 wt% Pt), Pt foil, and  $\text{PtO}_2$  powder. (b) Pt  $L_{3}$ -edge XANES spectra of  $\text{Pt}_{17}(\text{CO})_{12}(\text{PPh}_3)_8/\text{CB}$  (1.0 wt% Pt),  $\text{Pt}_{17}/\text{CB}$  (1.0 wt% Pt), Pt foil, and  $\text{PtO}_2$  powder. In (a), the Pt  $L_{3}$ -edge FT-EXAFS spectrum of  $\text{Pt}_{17}(\text{CO})_{12}(\text{PPh}_3)_8$ ,  $\text{Pt}_{17}(\text{CO})_{12}(\text{PPh}_3)_8/\text{CB}$  (1.0 wt% Pt) and  $\text{Pt}_{17}/\text{CB}$  (1.0 wt% Pt) have overall similarity to each other although there are small shifts in the peak positions, implying that the  $\text{Pt}_{17}$  framework is kept during the adsorption and calcination processes.

mass activity ( $182\text{ A g}^{-1}$  for  $0.9\text{ V}$ ) close to that reported in the literature for commercial Pt NPs/CB (46.9 wt% Pt) (Fig. S24†).

Fig. 5 shows the LSV curves of  $\text{Pt}_{17}/\text{CB}$  (1.0 wt% Pt)-EC and Pt NPs/CB (1.0 wt% Pt)-EC (prepared by mixing Pt NPs/CB (46.9 wt% Pt) and CB).  $\text{Pt}_{17}/\text{CB}$  (1.0 wt% Pt)-EC begins to generate a current at a lower overvoltage than Pt NPs/CB (1.0 wt% Pt)-EC and shows a higher current value at the same overvoltage (Tables S3 and S4†). These results indicate that  $\text{Pt}_{17}/\text{CB}$  (1.0 wt% Pt)-EC has higher ORR activity than Pt NPs/CB (1.0 wt% Pt)-EC. A comparison of the mass activity at  $0.9\text{ V}$  showed that the former had 2.1 times higher mass activity than the latter ( $145$  vs.  $68\text{ A g}^{-1}$  at  $0.9\text{ V}$ ).

In the above experiment, the Pt loading was set at 1.0 wt% to control the loading amount. This small amount of Pt on the catalyst results in fewer contacts between Pt NPs/CB and  $\text{O}_2$ , leading to a lower mass activity when compared with those dis-



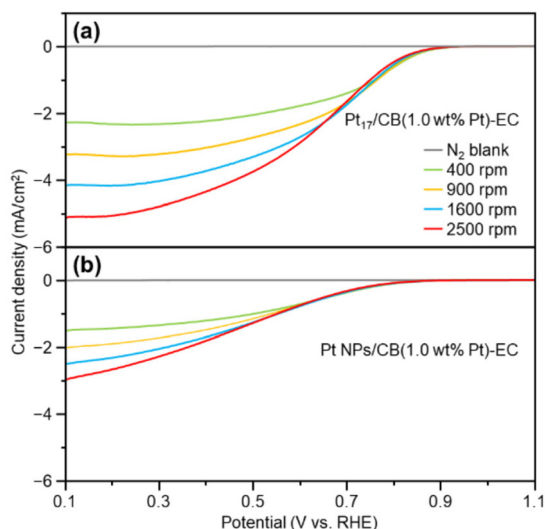


**Fig. 5** Comparison of LSV curves of the samples. (a)  $\text{Pt}_{17}/\text{CB}(1.0 \text{ wt\% Pt})\text{-EC}$ . (b)  $\text{Pt NPs}/\text{CB}(1.0 \text{ wt\% Pt})\text{-EC}$ . LSV curves were obtained for electrode rotation speeds of 400–2500 rpm under  $\text{O}_2$  gas. Measurements under  $\text{N}_2$  gas were conducted for baseline comparison. In these measurements, Pt loading was set to  $0.204 \mu\text{g cm}^{-2}$ .

played by catalysts with higher loadings of Pt.<sup>47</sup> Therefore, we have also prepared the  $\text{Pt}_{17}/\text{CB}(20.0 \text{ wt\% Pt})\text{-EC}$  on which 20.0 wt% Pt was loaded on CB (Fig. S25†). The electrochemical experiments on this catalyst confirmed that (1) the increase of Pt loading actually leads to the increase of the mass activity (Fig. S26(a)†;  $518 \text{ A g}^{-1}$  for 0.9 V), (2) 4-electron reduction occurs in  $\text{Pt}_{17}/\text{CB}(20.0 \text{ wt\% Pt})\text{-EC}$  (Fig. S26(b) and (c)†), similar to the case of  $\text{Pt NPs}/\text{CB}(46.9 \text{ wt\% Pt})$  (Fig. S24†), and (3)  $\text{Pt}_{17}/\text{CB}(20.0 \text{ wt\% Pt})\text{-EC}$  exhibits higher durability than commercial  $\text{Pt NPs}/\text{CB}$  (46.9 wt% Pt) (Fig. S27†).

### Origin of high activity of $\text{Pt}_{17}/\text{CB}$

We also investigated the origin of the high ORR activity exhibited by  $\text{Pt}_{17}/\text{CB}(1.0 \text{ wt\% Pt})$ . In elucidating the factor responsible for the increase in ORR activity due to the miniaturization of Pt NPs, generally, the electrochemical surface area (ECSA) is first estimated and then the specific activity (SA) is calculated based on the value of ECSA.<sup>48</sup> Using these two values (ECSA and SA), the main factor causing the difference in activity has been investigated: the increase in the percentage of surface Pt atoms or the improvement in the activity of each surface Pt atom. However, in such ECSA estimation, there is an assumption that the same charge flows regardless of the adsorption sites of  $\text{H}_2$  on Pt NPs. In reality, the charge flowing through the adsorption sites of  $\text{H}_2$  depends on the surface Pt atoms.<sup>49</sup> In addition, the surface of the Pt NCs supported on CB does not necessarily consist of only one type of surface structure.<sup>50</sup> Therefore, a discussion on the factors contributing to the differences in activity shown by the catalysts based solely on ECSA and SA calculated on the basis of these assumptions may not necessarily lead to a correct interpretation.

Literature studies have reported that (1) miniaturization induces the generation of surface Pt atoms with various charge/electronic states, and (2) high ORR activity is induced when the generated surface Pt atoms contain Pt atoms suitable for ORR progression.<sup>51,52</sup> Based on these facts, it is essential to clarify the charge and electronic states of each surface Pt atom involved in the reaction to gain a deeper understanding of the origin of the high ORR activity shown by  $\text{Pt}_{17}/\text{CB}$ . XANES (Fig. 4(b)) and XPS experiments can reveal the overall charge state of Pt NCs, but it is difficult to reveal the charge and electronic state of each surface Pt atom using these experiments. Therefore, in the present study, we estimated the charge and electronic states of each surface Pt atom in  $\text{Pt}_{17}/\text{CB}$  by DFT calculations. To reduce computational cost, a graphite structure,<sup>53</sup> which is well understood, was used for the carbon support structure instead of CB structure. We obtained the optimized structure of  $\text{Pt}_{17}/\text{graphite}$  by structural optimization using the structure of supported  $\text{Pt}_{17}$  observed by HAADF-STEM in our previous study<sup>14</sup> as the initial structure (Fig. S28†).

Fig. 6(a) shows the optimized structure obtained for  $\text{Pt}_{17}/\text{graphite}$  (Fig. S29†). In this geometry, 15 Pt atoms are located on the surface and two Pt atoms ( $i = 6$  and  $12$ ) are in contact with graphite. Fig. 6(b) shows the charge of each Pt atom. Pt in contact with graphite ( $i = 6$  and  $12$ ) is positively charged. This positive charging is slightly enhanced by the charge transfer from Pt to graphite (Fig. S30†).<sup>13</sup> The Pt atoms located on the terrace ( $i = 1, 4, 7$ , and  $17$ ) are also positively charged. In contrast, the Pt atoms ( $i = 2, 3, 5, 8\text{--}11$  and  $13\text{--}16$ ) located at the steps and corners are negatively charged. Thus, each Pt atom in  $\text{Pt}_{17}/\text{graphite}$  has a different charge depending on its position in  $\text{Pt}_{17}$ . Analysis of the local density of electronic states (LDOS) also revealed that each Pt atom has a different LDOS (Fig. S31†). These results indicate that Pt atoms with various charges and LDOS are present in  $\text{Pt}_{17}/\text{carbon support}$ .<sup>4,54</sup> We also considered the possibility of residual CO being on  $\text{Pt}_{17}$  and thereby performed the same structural optimization and charge and LDOS estimation at each Pt atom ( $\text{CO}/\text{Pt}_{17}/\text{graphite}$ ) in  $\text{Pt}_{17}/\text{graphite}$  with one CO adsorbed on the  $\text{Pt}_{17}$  surface. The results suggest that Pt atoms of various charges and LDOS are also present in  $\text{CO}/\text{Pt}_{17}/\text{graphite}$ , similar to the case of  $\text{Pt}_{17}/\text{graphite}$  (Fig. S32 and S33†).

To gain insight into the ORR on  $\text{Pt}_{17}$  NC surfaces consisting of Pt with various charges and LDOS, we performed structural optimization for the reaction intermediates in the ORR. For the adsorption sites of  $\text{O}_2$ , four pairs of Pt atoms were selected as shown in Fig. 6(a) ( $\text{Pt}_{17}/\text{graphite}(\text{X})$ ;  $\text{X} = \text{A, B, C, or D}$ ; Fig. S34†). The structure of the subsequent reaction intermediate was estimated by adsorbing H on the obtained structure (Fig. S35†). The results suggest the following: (1) when  $\text{O}_2$  is adsorbed on  $\text{Pt}_{17}/\text{graphite}(\text{X})$  ( $\text{X} = \text{A, B, C, or D}$ ) ( $\text{O}_2/\text{Pt}_{17}/\text{graphite}(\text{X})$ ), the O–O bond of the adsorbed  $\text{O}_2$  is elongated regardless of the adsorption sites (Fig. 6(c) and S34 and Table S5†); (2) when H is adsorbed on such structures, the O–O bond of the adsorbed  $\text{O}_2$  dissociates readily (Fig. 6(d) and S35 and Table S6†); and (3) therefore, unlike the  $\text{Pt}(111)$  surface, the



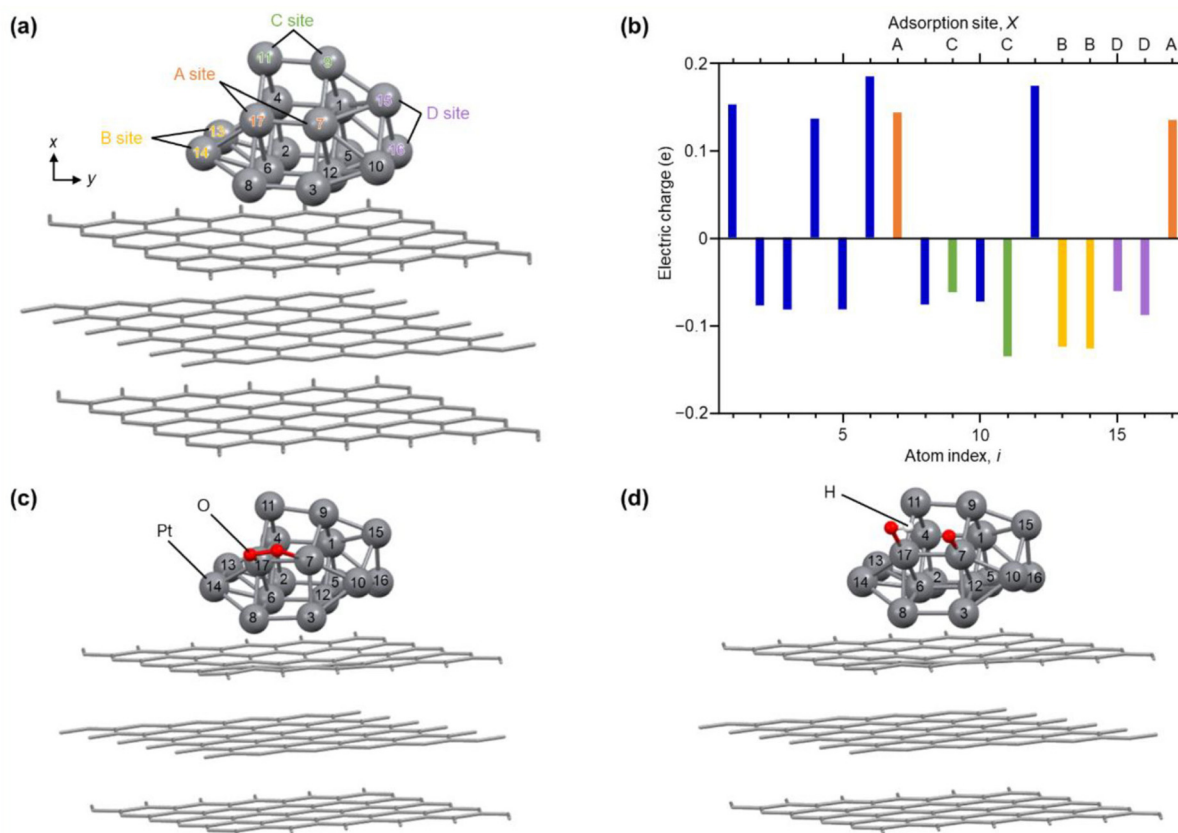


**Fig. 6** Results of DFT calculations. (a) Optimized structure of each Pt atom in Pt<sub>17</sub>/graphite. The atom index (*i*) of each Pt atom and site (A–D) involved in reaction with O<sub>2</sub> are also described. (b) Electric charge of each Pt atom in Pt<sub>17</sub>/graphite. (c) Intermediate structure optimized for O<sub>2</sub>/Pt<sub>17</sub>/graphite(A). (d) Intermediate structure optimized for (O + OH)/Pt<sub>17</sub>/graphite(A). The other intermediate structures, O<sub>2</sub>/Pt<sub>17</sub>/graphite(X) and (O + OH)/Pt<sub>17</sub>/graphite(X) (X = B, C, or D), are shown in Fig. S32 and S33.†

adsorption of O and OH, but not OOH, occurs on the Pt<sub>17</sub> surface (Fig. 6(d) and Fig. S35;† (O + OH)/Pt<sub>17</sub>/graphite(X); X = A, B, C, or D). Overall, these results are in good agreement with the results of the DFT calculations on Pt<sub>13</sub>/graphite reported by Lim and Wilcox.<sup>13</sup>

Fig. 7 shows the energy diagram<sup>55</sup> of the ORR when a voltage of 0.9 V is applied. For comparison, Fig. 7 also shows the energy diagram of ORR on Pt(111) surface, which is included in Pt NPs/CB(46.9 wt% Pt)<sup>56</sup> (each intermediate is O<sub>2</sub>/Pt(111), OOH/Pt(111), and (O + OH)/Pt(111)). All O<sub>2</sub>/Pt<sub>17</sub>/graphite(X) are more energetically stable than O<sub>2</sub>/Pt(111) because Pt in the Pt NCs forms stronger bonds with O than Pt on the Pt(111) surface.<sup>13</sup> However, comparison of the four O<sub>2</sub>/Pt<sub>17</sub>/graphite(X) reveals that such stabilization is not so large for O<sub>2</sub>/Pt<sub>17</sub>/graphite(X) (X = A or C). The (O + OH)/Pt<sub>17</sub>/graphite(A) generated upon reaction at site A had the same potential as (O + OH)/Pt(111)/graphite(A). These results imply that the ORR proceeds at site A under an applied voltage of 0.9 V, similarly to Pt(111).

Further investigation of the results also revealed some differences between Pt<sub>17</sub>/graphite(A) and Pt(111). The most striking difference is that the process from O<sub>2</sub>/Pt<sub>17</sub>/graphite(A) to (O + OH)/Pt<sub>17</sub>/graphite(A) involves a moderate uphill reac-

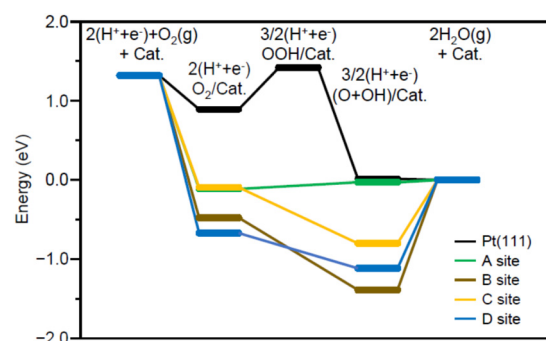


**Fig. 7** Free-energy diagram for ORR through a direct four-electron pathway on Pt<sub>17</sub>/graphite(X) (X = A, B, C, or D) or Pt(111) under an applied potential of 0.9 V. In this figure, Pt<sub>17</sub>/graphite(X) (X = A or B) and Pt(111) are abbreviated as Cat.

tion, whereas the process from O<sub>2</sub>/Pt(111) to (O + OH)/Pt(111) involves sharp uphill reactions (O<sub>2</sub>/Pt(111) → OOH/Pt(111)). This means that ORR progresses more readily on Pt<sub>17</sub>/graphite (A) than on Pt(111) surface. This is considered to be a reason why Pt<sub>17</sub>/CB(1.0 wt% Pt) shows higher ORR activity than Pt NPs/CB(1.0 wt% Pt).







- 19 B.-J. Hwang, L. S. Sarma, C.-H. Chen, C. Bock, F.-J. Lai, S.-H. Chang, S.-C. Yen, D.-G. Liu, H.-S. Sheu and J.-F. Lee, *J. Phys. Chem. C*, 2008, **112**, 19922–19929.
- 20 I. Schrader, J. Warneke, S. Neumann, S. Grotheer, A. A. Swane, J. J. K. Kirkensgaard, M. Arenz and S. Kunz, *J. Phys. Chem. C*, 2015, **119**, 17655–17661.
- 21 J. Wei, R. Marchal, D. Astruc, S. Kahlal, J.-F. Halet and J.-Y. Saillard, *Nanoscale*, 2022, **14**, 3946–3957.
- 22 C. Femoni, M. C. Iapalucci, G. Longoni, S. Zacchini and S. Zarra, *J. Am. Chem. Soc.*, 2011, **133**, 2406–2409.
- 23 S. Antonello, N. V. Perera, M. Ruzzi, J. A. Gascón and F. Maran, *J. Am. Chem. Soc.*, 2013, **135**, 15585–15594.
- 24 M. Zhu, C. M. Aikens, M. P. Hendrich, R. Gupta, H. Qian, G. C. Schatz and R. Jin, *J. Am. Chem. Soc.*, 2009, **131**, 2490–2492.
- 25 M. A. Tofanelli, K. Salorinne, T. W. Ni, S. Malola, B. Newell, B. Phillips, H. Häkkinen and C. J. Ackerson, *Chem. Sci.*, 2016, **7**, 1882–1890.
- 26 Y. Shichibu and K. Konishi, *Small*, 2010, **6**, 1216–1220.
- 27 B. K. Teo and H. Zhang, *Coord. Chem. Rev.*, 1995, **143**, 611–636.
- 28 N. Yan, N. Xia, L. Liao, M. Zhu, F. Jin, R. Jin and Z. Wu, *Sci. Adv.*, 2018, **4**, eaat7259.
- 29 Y. Negishi, W. Kurashige, Y. Niihori, T. Iwasa and K. Nobusada, *Phys. Chem. Chem. Phys.*, 2010, **12**, 6219–6225.
- 30 E. Ito, S. Takano, T. Nakamura and T. Tsukuda, *Angew. Chem., Int. Ed.*, 2021, **60**, 645–649.
- 31 M. Laupp and J. Strähle, *Angew. Chem., Int. Ed. Engl.*, 1994, **33**, 207–209.
- 32 M. Akutsu, K. Koyasu, J. Atobe, N. Hosoya, K. Miyajima, M. Mitsui and A. Nakajima, *J. Phys. Chem. A*, 2006, **110**, 12073–12076.
- 33 D. Tashima, H. Yoshitama, M. Otsubo, S. Maeno and Y. Nagasawa, *Electrochim. Acta*, 2011, **56**, 8941–8946.
- 34 T. Kawawaki, N. Shimizu, K. Funai, Y. Mitomi, S. Hossain, S. Kikkawa, D. J. Osborn, S. Yamazoe, G. F. Metha and Y. Negishi, *Nanoscale*, 2021, **13**, 14679–14687.
- 35 T. Kawawaki, Y. Kataoka, M. Hirata, Y. Iwamatsu, S. Hossain and Y. Negishi, *Nanoscale Horiz.*, 2021, **6**, 409–448.
- 36 T. Kawawaki, Y. Kataoka, M. Hirata, Y. Akinaga, R. Takahata, K. Wakamatsu, Y. Fujiki, M. Kataoka, S. Kikkawa, A. S. Alotabi, S. Hossain, D. J. Osborn, T. Teranishi, G. G. Andersson, G. F. Metha, S. Yamazoe and Y. Negishi, *Angew. Chem., Int. Ed.*, 2021, **60**, 21340–21350.
- 37 T. Kawawaki, Y. Kataoka, S. Ozaki, M. Kawachi, M. Hirata and Y. Negishi, *Chem. Commun.*, 2021, **57**, 417–440.
- 38 D. P. Anderson, J. F. Alvino, A. Gentleman, H. Al Qahtani, L. Thomsen, M. I. J. Polson, G. F. Metha, V. B. Golovko and G. G. Andersson, *Phys. Chem. Chem. Phys.*, 2013, **15**, 3917–3929.
- 39 D. P. Anderson, R. H. Adnan, J. F. Alvino, O. Shipper, B. Donoeva, J.-Y. Ruzicka, H. Al Qahtani, H. H. Harris, B. Cowie, J. B. Aitken, V. B. Golovko, G. F. Metha and G. G. Andersson, *Phys. Chem. Chem. Phys.*, 2013, **15**, 14806–14813.
- 40 Y. Lu, Y. Jiang, X. Gao and W. Chen, *Chem. Commun.*, 2014, **50**, 8464–8467.
- 41 L. Lu, S. Zou, Y. Zhou, J. Liu, R. Li, Z. Xu, L. Xiao and J. Fan, *Catal. Sci. Technol.*, 2018, **8**, 746–754.
- 42 Z. Peng and H. Yang, *J. Am. Chem. Soc.*, 2009, **131**, 7542–7543.
- 43 L. Wang, Z. Tang, W. Yan, H. Yang, Q. Wang and S. Chen, *ACS Appl. Mater. Interfaces*, 2016, **8**, 20635–20641.
- 44 L. Sumner, N. A. Sakthivel, H. Schrock, K. Artyushkova, A. Dass and S. Chakraborty, *J. Phys. Chem. C*, 2018, **122**, 24809–24817.
- 45 G. Samjeské, S.-i. Nagamatsu, S. Takao, K. Nagasawa, Y. Imaizumi, O. Sekizawa, T. Yamamoto, Y. Uemura, T. Uruga and Y. Iwasawa, *Phys. Chem. Chem. Phys.*, 2013, **15**, 17208–17218.
- 46 M. Mench, E. C. Kumbur and T. N. Veziroglu, *Polymer electrolyte fuel cell degradation*, Academic Press, Cambridge, 2011.
- 47 S. H. Joo, K. Kwon, D. J. You, C. Pak, H. Chang and J. M. Kim, *Electrochim. Acta*, 2009, **54**, 5746–5753.
- 48 M. Shao, A. Peles and K. Shoemaker, *Nano Lett.*, 2011, **11**, 3714–3719.
- 49 H. Ogasawara and M. Ito, *Chem. Phys. Lett.*, 1994, **221**, 213–218.
- 50 R. K. Bera, H. Park, S. H. Ko and R. Ryoo, *RSC Adv.*, 2020, **10**, 32290–32295.
- 51 F. Calle-Vallejo, J. Tymoczko, V. Colic, Q. H. Vu, M. D. Pohl, K. Morgenstern, D. Loffreda, P. Sautet, W. Schuhmann and A. S. Bandarenka, *Science*, 2015, **350**, 185–189.
- 52 B. Garlyyev, J. Fichtner, O. Piqué, O. Schneider, A. S. Bandarenka and F. Calle-Vallejo, *Chem. Sci.*, 2019, **10**, 8060–8075.
- 53 D. Tománek and S. G. Louie, *Phys. Rev. B: Condens. Matter Mater. Phys.*, 1988, **37**, 8327–8336.
- 54 G. Ramos-Sanchez and P. B. Balbuena, *Phys. Chem. Chem. Phys.*, 2013, **15**, 11950–11959.
- 55 H. A. Hansen, J. Rossmeisl and J. K. Nørskov, *Phys. Chem. Chem. Phys.*, 2008, **10**, 3722–3730.
- 56 K. i. Miyazawa, S. Shimomura, M. Yoshitake and Y. Tanaka, *Int. J. Eng. Res. Ind. Appl.*, 2018, **8**, 13–21.
- 57 W. Kurashige, R. Hayashi, K. Wakamatsu, Y. Kataoka, S. Hossain, A. Iwase, A. Kudo, S. Yamazoe and Y. Negishi, *ACS Appl. Energy Mater.*, 2019, **2**, 4175–4187.
- 58 L. K. Batchelor, B. Berti, C. Cesari, I. Ciabatti, P. J. Dyson, C. Femoni, M. C. Iapalucci, M. Mor, S. Ruggieri and S. Zacchini, *Dalton Trans.*, 2018, **47**, 4467–4477.

